Transitions and oscillations in a thermohaline deep ocean circulation model

J. A. Whitehead

Published online: 10 Oct 2018.

Submit your article to this journal 🗗

Article views: 96

View related articles 🗗

View Crossmark data 🗗

Taylor & Francis
Taylor & Francis Group

Check for updates

ransitions and oscillations in a thermohaline deep ocean circulation model

J. A. Whitehead

Department of Physical Oceanography, Woods Hole Oceanographic Institution, Woods Hole, MA, USA

BSTR CT

Theoretical ocean convection is a numerically calculated model of the ocean with salt water in a two-dimensional container. The boundary conditions along the top are linearly changing temperature T and flux of salinity S increasing from the model's pole to equator. The sides and bottom are insulated and impermeable. Diffusivities of T and S are equal so double diffusion is eliminated. Therefore, the focus is upon the consequences of mixed Dirichlet/Neumann conditions upon two-dimensional T/S convection in this deep ocean overturning circulation configuration. Results are calculated over wide ranges of Rayleigh number Ra (0–2 $\times 10^6$), salinity flux Rayleigh number Raf (0–3 $\times 10^6$), container length (2–32), and Prandtl number r (1–128 and ∞). Two different equations of state are considered: one has constant properties everywhere including constant thermal and salinity density coefficients (the Boussinesq approximation), and the second uses the seawater equation of state in an oceanic T–S range. Results at fixed Ra are presented for numerous values of Raf until either a steady flow or a time-dependent cyclic flow sets in. For Boussinesq flow with $r < 10$, and for seawater flow up to at least $r = 128$, flow oscillates in some parameter ranges. The oscillation of convection cells occurs during a salinity dominated mode with equatorial sinking. This oscillation differs from oscillations of the temperature dominated mode in some climate models and it also differs from oscillations in laboratory experiments for T/S driven convection. In other parameter ranges, flows become steady and hysteresis and multiple states exist for the two modes.

1 Introduction

The flows of heat and of water in and out of the ocean surface provide boundary conditions to the ocean's temperature and salinity that have profound effects on deep ocean circulation, equator to pole heat transfer, atmospheric weather and earth's climate. A classic model that is more than 50 years old (Stommel 1961) illustrates the very simplest consequence of the fact that there might be different time scales for buoyancy forcing from temperature and salinity. Although deep ocean water is cold as a result of convective sinking in the

Earth's colder regions it showed that another mode of ocean flow is possible, with sinking in regions of enhanced salinity by excess evaporation over precipitation (*E–P*). The model consists of two chambers containing stirred water placed side by side and connected by two lateral tubes, one at the top and another at the bottom. Each chamber has a small stirrer and a diffusive, conductive sidewall in contact with a neighbouring storage tank. One storage tank contains hot salty water to represent heating and excess (*E–P*) over the tropical ocean. The other storage tank contains cold water of lower salinity to represent cooling and negative (*E–P*) over a polar region. The model is frequently referred to as a "box model" since the chambers and tubes can be represented as boxes of water connected by tubes. The governing parameters are the difference of storage tank temperatures T^*, and salinities S^*, the diffusion rates of T and S through the diffusive, conductive sidewalls and drag within the tubes. They form the ratio $\alpha T^*/\beta S^*$ (α is coefficient of thermal expansion and β is the density change coefficient for salinity), a thermal timescale τ_T, a salinity timescale τ_S, and an expression of the drag experienced by the water flowing between chambers. For the ocean, $\tau_T < \tau_S$ and hysteresis occurs between one flow dominated by T (the T-mode, with sinking in the cold freshened box), to a second flow dominated by S (the S-mode, with sinking in the warm salty box) as long as drag is sufficiently small. Subsequent studies of more complex box models also find multiple states and hysteresis between them (Marotzke 1994). The box model has similar results if salinity relaxation with timescale τ_S is replaced by salinity flux (Whitehead 1995, 1996).

Flow driven by temperature differences and salinity flux is the topic of this study. It has been found that oscillations can also occur for flows driven by different flux laws for temperature and salinity at a surface. A simple model by Welander (1982) considers a stratified region of fluid below a horizontal surface kept at constant temperature and with a constant flux of salinity with two stacked boxes and different diffusion rules between the boxes depending on the density jump. An oscillation occurs for certain parameters. A second model (Welander 1989) is a more realistic case of a small perturbation to stratified fluid with constant salinity flux at the top surface. If an isopycnic surface below the top is displaced upward by a small amount, the value of heat flow at the boundary is altered because the local temperature gradient increases but salt flux is constant. This produces a phase lag leading to growing oscillations. Although the mechanism resembles "double-diffusion" oscillations when the diffusivities of two substances differ, (Turner 1973), this oscillation occurs even if the diffusivities are the same.

Laboratory experiments with fixed temperature differences and salt flux imposed by a pump have produced both hysteresis and oscillations. The earliest experiments had a geometry like the Stommel box model with some variations for practical reasons. For one thing, steadily pumped salty and fresher waters was a useful replacement to the diffusion of salinity through the sidewalls because experiment duration was reduced from days to tens of minutes. The magnitudes of hysteresis and of the jumps agree with a theory modified for the laboratory configuration (Whitehead, 1995, 1996, 1998, 2000). Another design exhibits only a tiny hysteresis range in spite of the fact that the jumps between modes remains large (Whitehead 2009). Yet another design develops an oscillation with a layer that forms and mixes away periodically (te Raa 2001, Whitehead *et al.* 2005). It is perhaps a good finite amplitude expression of Welander's (1982) "*flip-flop*".

This study pursues the quest to find multiple states and finite amplitude oscillations using the Navier-Stokes equations in the simplest possible configuration, a simple

rectangular container. The convection is driven by an oceanlike linearly changing top surface temperature boundary condition (Dirichlet boundary condition), found in a number of configurations to study dynamics of deep ocean sinking (Rossby 1965, Beardsley and Festa 1972, Paparella and Young 2002, Winters and Young 2009). Superimposed on the top Dirichlet temperature condition is salinity flux along the top (representing water flux) with positive salinity flux at the hot end that linearly decreases to negative salinity flux at the cold end (Neumann boundary condition). Along the sides and bottom the container is insulated and has zero salinity flux. The internal mixing properties of T and S are set equal to each other. Such a mixing law is like most numerical models that assign equal values for turbulent stirring of T and S within the ocean. It eliminates double-diffusion at the boundaries and certain well-known consequences such as salt fingers or double-diffusive layers within the fluid. Therefore, this model is probably the simplest one possible. Calculations with this simple geometry are not previously completed over extensive parameter ranges.

The initial motivation for the calculations was to document the expected multiple states and hysteresis as in Stommel's box model and the laboratory results. Subsequent justification arose after connections with ocean models became clear. Specifically, a wide range of such ocean circulation models exhibits oscillations. In many cases, a variety of mechanisms are included in such models such as atmospheric variability, rotating dynamics, instability leading to eddies and turbulence, wind effects, and ice (Sakai and Peltier 1996, Timmermann *et al.* 2003, Loving and Vallis 2005, Arzel *et al.* 2006, Sevellec and Fedorov 2015 and references therein). Ocean circulation models relevant to the present study use only evaporation minus precipitation salinity balances combined with a fixed atmospheric temperature. Phase lags of T and S generate oscillations in the Atlantic meridional overturning circulation. The models have varied complexity and sophistication. A simple 3 × 2 box model (Colin de Verdière, Jelloul, and Sèvellec 2006) combines the abrupt transitions of the Stommel model with the "*flip-flop* oscillations found by Welander (1982)". Oscillations also exist in a simple box model (Colin de Verdière 2007), a two-dimensional ocean circulation model (Sevellec *et al.* 2006, Marchal *et al.* 2007), a three-dimensional general circulation ocean model (Weaver and Sarachik 1991, Weaver *et al.* 1993), and coupled ocean-atmospheric climate models (Delworth *et al.* 1993, Arzel *et al.* 2010, Colin de Verdière and te Raa 2010, and references therein). Oscillation periods are typically millennial. Without exception, there are cyclic changes in strength of the T-mode (corresponding to the present North Atlantic circulation). An oscillating S-mode is not found.

It must be emphasised that the intent here is not to provide an ocean model. Too much important dynamics is missing. Principally, in this first approximation, the equations for a rotating fluid are not even used. Why is rotation omitted when it is an essential ingredient of most ocean models? The answer is twofold. First, the equations of motion for rotating fluid, especially those applied to the ocean are more complex. They require either a fully three-dimensional container or an averaging procedure across the basins to produce simplified (zonally averaged) circulation, but this requires assumptions about dissipation within the western boundaries and sinking regions that are not yet proven. Second, it is useful to strip the problem down to the simplest case to study first. We can show that our results are robust features over a much wider range of parameters than those of ocean model projects.

In addition, ocean circulation is only one of many phenomena represented by the box. Oscillations are already found in other containers using Dirichlet/Neumann boundary conditions. One sequence of studies of oscillating flows involves containers with binary

convection driven by mixed Dirichlet/Neumann conditions (Tsitverblit, 1995, 1997a), and in tilted slots (Tsitverblit 1997b, 1999, 2004, 2007, Zhao *et al.* 2007). Another study has oscillations in a single cell model of Rayleigh–Benard convection of water driven by a temperature difference and an upward flux of salinity (Whitehead 2017). Therefore, numerous studies with mixed Neumann/Dirichlet forcing reinforced the idea that multiple equilibria and oscillations might arise in the simplest problem as it is formulated here.

Although emphasis in this introduction is on an ocean model, abrupt transitions and oscillations from mixed Dirichlet/Neumann might also occur in situations other than the ocean. Multicomponent convection with mixed boundary conditions might occur in other regions in the earth, as well as in the planets, in some of their moons, in certain types of stars and in engineering. Virtually every fluid is multicomponent in the natural world. Earth's atmosphere and the gaseous planets have both temperature and another component such as water, carbon dioxide, hydrogen or helium. Numerous moons have water and possibly dissolved components with active interaction with ice melting and freezing. Likewise, Earth has many layers of the surface, mantle, and core, all with a fixed surface temperature and a compositional flux of water, crust and sediment into and out of the interior. Finally, the stars have temperature and helium/hydrogen ratios, with differing flux laws between layers. Thus, it is hoped that for all the reasons listed in this introduction, the focus upon the consequences of mixed Dirichlet, Neumann double component convection with such a simple geometry is justified by the new results presented here.

2   The model and governing equations

Convection in a container of water is driven by a temperature and salinity flux distributed across the top. The water salinity S_0 lies in a rectangular container of depth D, where z is positive upward in the vertical direction of gravity and of length L in the lateral (x) direction along the container. The average initial temperature of the fluid is T_0. A temperature $T_0 - (\Delta T/2)$ increases linearly from the top of the left end to $T_0 + (\Delta T/2)$ at the top of the right end. This makes the densest water from T at the left end and lightest at the right. A downward salinity flux $F_S = \kappa[\partial S/\partial z]$ is also imposed, where κ is salt diffusivity. (Note this definition of flux differs from the usual definition, which would apply to flux in the upward direction.) The imposed downward flux at the top of the container is the negative of this value at the left end and it linearly increases to this value at the right end. Therefore, the densest water from S is at the right end and the lightest at the left.

The equations governing conservation of mass, momentum, heat, and salt have constant coefficients except for terms driven by buoyancy (see Appendix). They are transformed to dimensionless form using velocity scale κ/D, temperature scale ΔT (temperature in deviation from T_0), a salinity scale based on the gradient providing a flux to the flow at the right-hand top $\Delta S = 2D\partial S/\partial z_{0,L}$, and the timescale D^2/κ. The dimensionless container is sketched in figure 1. Dimensionless salinity flux along the top ranges from -0.5 to 0.5 and dimensionless temperature ranges from 0 to 1. The container has depth 1 and a length given by the length L/D.

The dimensionless equations are

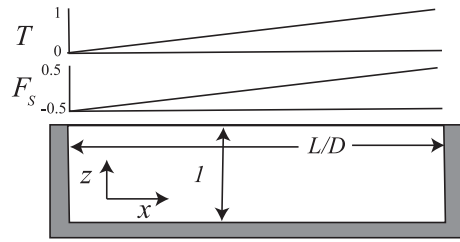$$\frac{\partial T}{\partial t} + \quad \nabla T = \nabla^2 T, \tag{1}$$

Figure 1 A two-dimensional insulated rectangular container of water has linear changes of T and downward salt flux F_S along the top. There is zero flux of water, heat and salt through the sides and bottom.

$$\frac{\partial S}{\partial t} + \quad \nabla S = \nabla^2 S. \tag{2}$$

Only two-dimensional flows are considered. The vorticity equation is

$$\left[\frac{1}{Pr} \frac{\partial}{\partial t} + \quad \nabla \right) - \nabla^2 \right] \zeta = Ra\frac{\partial T}{\partial x} - Raf\frac{\partial S}{\partial x}, \tag{3}$$

where $\zeta = (\partial u/\partial z) - (\partial w/\partial x)$. The equation for a streamfunction is

$$\nabla^2 \psi = \zeta. \tag{4}$$

The three governing parameters are the Rayleigh number $Ra = g \ \Delta T D^3/\kappa\nu$, the salinity flux Rayleigh number $Raf = -g\beta[\partial S/\partial z]D^4/\kappa\nu$ and the Prandtl number $Pr = \nu/\kappa$ where ρ_0 is average density, ν is kinematic viscosity, g is acceleration of gravity, is the coefficient of thermal expansion, β is the coefficient of density change by salinity, and κ is both thermal and salinity diffusivity. Length L/D is a fourth dimensionless number.

The appendix contains a description of the procedure of integration and tests of the finite difference scheme used to numerically advance equations (1)–(4) in time t. The most novel results, described in section 3, are oscillations that are different from ones found in other configurations. The results show that with Boussinesq equations (i.e. with constant and β), the oscillations occur over broad ranges of L/D, Ra, and Raf for $Pr < 4$. Oscillations also occur with a seawater equation of state for Pr from 1 to 128. The standard formula EOS-80 (SCOR working group 1979) for the coefficients of expansion for temperature and salinity for seawater is used with an average temperature of 5.0°C and salinity of 35 PSU. For seawater calculations, spatially dependent values of Ra and Raf are inserted at each grid point of the numerical equivalent to equation (3) to mimic the variation of expansion coefficients. The average values of Ra and Raf are used to set the parameter space results. Section 4 describes steady flows that occur for Boussinesq equations with $Pr = \infty$ and in one case the results are shown to be very similar for $Pr = 1$. Either a T-mode or an S-mode flow occurs with hysteresis and abrupt transition separating the extremes, similar to even simple box model results. The parameter spaces for steady flows that are determined are first a short container with $L/D = 2$ for $Pr = \infty$, and for $Pr = 1$ with either Ra below 10^5 and Raf below 8 10^5; or second for $L/D = 8$, 16, and 32 for values of Ra and Raf from 0 up to 2 10^6. The places that results are given and the parameter coverage are all listed in table 1.

Table 1 Numerical results.

Location	Ra	Raf	L/D	Pr	Type
Sec. 3	2×10^6	10^5 to 2×10^6	8,32	$1, \infty$	B, S
Sec. 5	2×10^6	0	2	1	B
2a	10^4	Up to 1.5×10^5	2	1	B
2b	3×10^4	Up to 3×10^5	2	1	B
2c	3×10^5	Up to 3×10^6	2	1	B
3a, 3e	10^5	Up to 8×10^5	8	1	B, S
3b, 3f	10^5	Up to 8×10^5	8	2	B, S
3c, 3g	10^5	Up to 8×10^5	8	3	B, S
3d, 3h	10^5	Up to 8×10^5	8	4	B, S
4	10^5	$3 \times 10^5, 2.5 \times 10^5$	8	16 to 128	S
5	10^5	3.5×10^5	8	10	S
6	10^5	2.5×10^5	8	1	S
7a	10^4	Up to 4×10^4	2	∞	B
7b	3×10^4	Up to 6.3×10^5	2	∞	B
7c	10^5	Up to 1.8×10^6	2	∞	B
8	3×10^4	6×10^5 to 59,100	2	∞	B
9	0	0	16	∞	B
10	1000	10	16	$1, \infty$	B
11	1000	50	16	∞	B
12a	3×10^4	Up to 8×10^4	8	∞	B
12b	5×10^5	Up to 3×10^6	8	∞	B
13	3×10^4	9200 to 11,600	8	∞	B
14	3×10^4	36,100 to 36,200	8	∞	B
15a	5×10^5	0	8	∞	B
15b	5×10^5	5×10^5	8	∞	B
15c	0	5×10^5	8	∞	B

Note: Type indicates the equation of state; B is for Boussinesq and S for Saltwater.

3   Oscillating flows at low Prandtl number and in seawater

The length $L/D = 2$ is useful for determining the behaviour of the competing thermal and salinity forcing because two circulating cells can lie side by side and each cell can be driven by T or S more strongly and yet numerous cells side-by-side are not possible. For $Ra = 10^4$ and $Pr = 1$, (figure 2(a)), hysteresis and abrupt transitions similar to the original Stommel box model occur. However, for the larger values $Ra = 3 \times 10^4$ and 10^5 and $Pr = 1$ (figure 2(b,c)) oscillations occur in place of a hysteresis range. The ranges shown in figure 2 are not precise. Runs with slowly varying control parameters don't accurately indicate the limits of the oscillation range since oscillations at transition can have very long growth or decay rates.

Similar oscillations exist in longer containers. Figure 3(a–d) (left column) presents results when each flow has come to an equilibrium value of either steady flow or an oscillation over many flow periods. It shows amplitude for the cases of Boussinesq convection at $Ra = 10^5$, $L/D = 8$ and for the four values $Pr = 1, 2, 3, 4$. Although coverage is not as complete as in figure 2 because of time limitations for the numerous computations, clearly there are well-defined ranges of oscillations for the first three values of Pr. The ranges of oscillations differ from the range of hysteresis for $Pr = 4$ in figure 3(d).

Ocean values of Pr extend from 4 in polar regions up to 13 in the tropics. Therefore, the Boussinesq results motivated calculations over the same parameter range with a seawater equation of state. Since the salinity-temperature dependent density relation for sea water is nonlinear, it was anticipated that time-dependent flows might be more prevalent. The calculations advance the vorticity equation in time based on values of Ra and Raf of
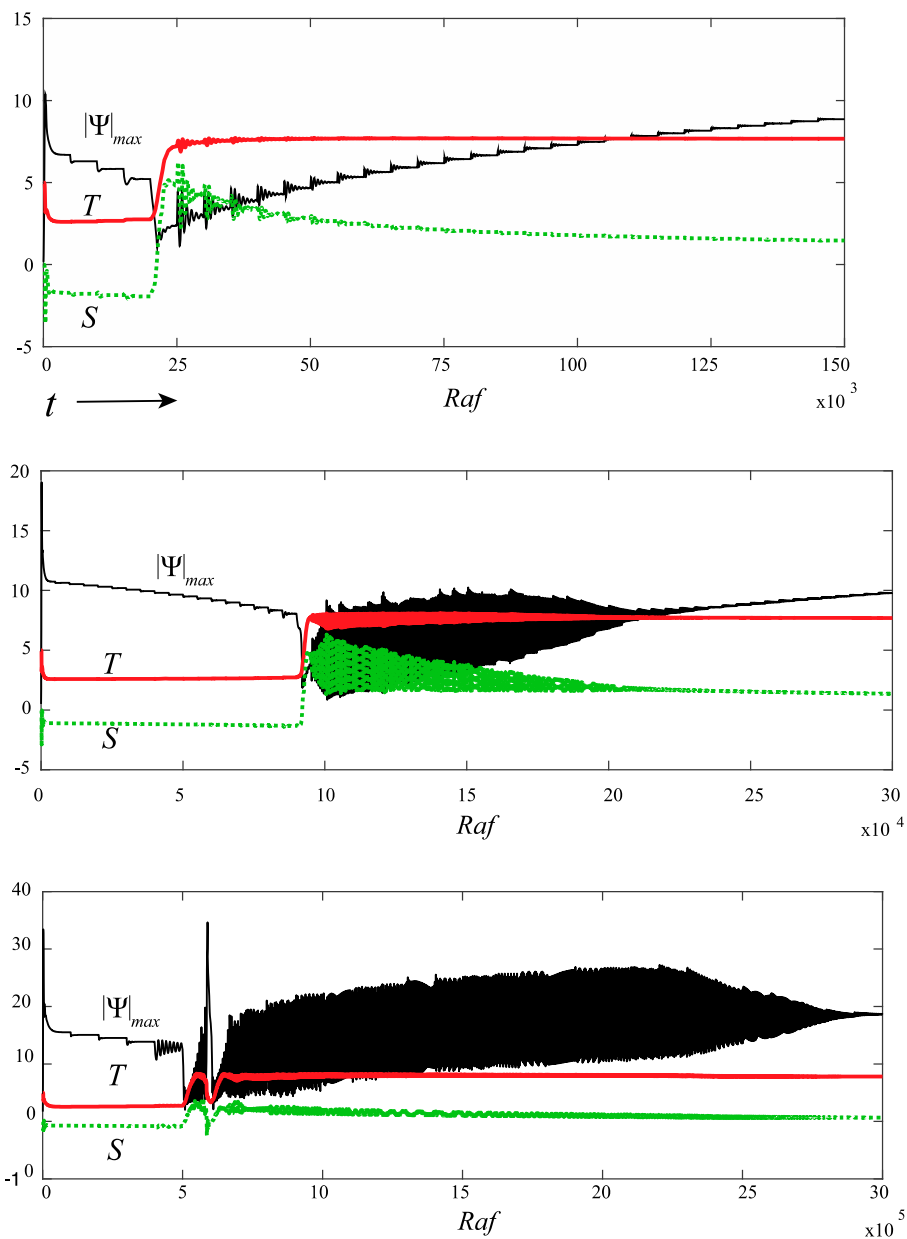
Figure 2 Evolution of the maximum absolute value of streamfunction $|\psi_{max}|$ (black, solid), T at the centre of the bottom multiplied by 10 (red, heavy) and S at the centre of the bottom multiplied by 100 (green, dots) for Boussinesq fluid with $Pr = 1$ and $L/D = 2$. Values of Raf are substituted for time because Raf is increased by fixed steps sequentially. (a) $Ra = 10^4$, Raf starts at 0 and increases in steps of 5000 up to 1.5 10^5. (b) $Ra = 3$ 10^4 with the same Raf sequence up to 3 10^5. (c) $Ra = 10^5$ with Raf starting at 0 and increasing in steps of 10^5 up to 3 10^6 (colour online).
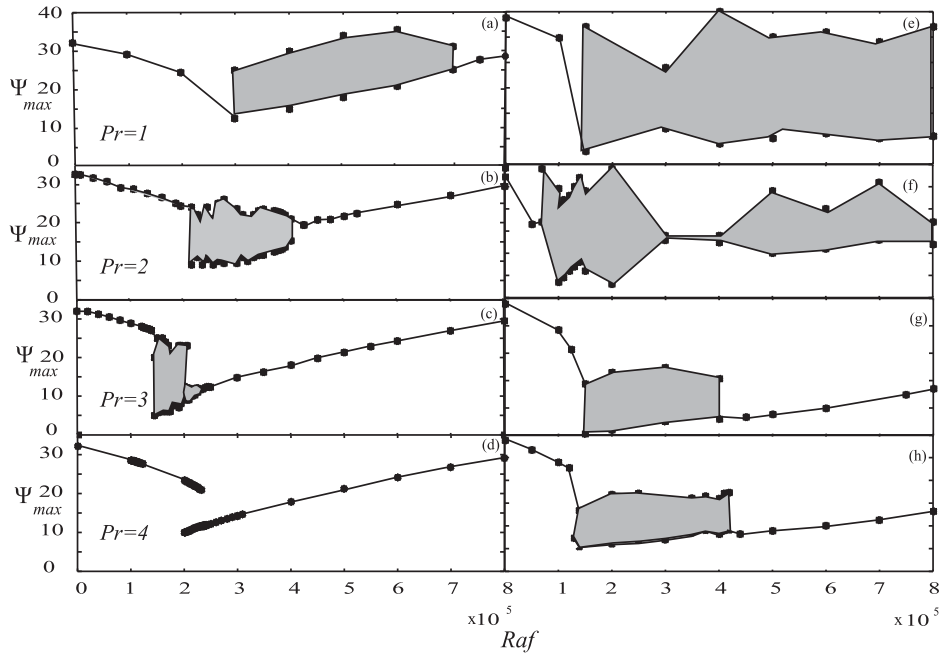
Figure 3 Value of streamfunction for convection at $Ra = 10^5$, $L/D = 8$. This is not a time sequence like figure 2. Each point represents the maximum or minimum for a long run over numerous cycles. The regions with time-dependent flow are shaded. Results are for Boussinesq equations on the left and for seawater polynomial coefficients on the right with (a,e) $Pr = 1$ (b, f) $Pr = 2$ (c, g) $Pr = 3$, (d, h) $Pr = 4$.

seawater at every grid point. The seawater equation of state is centred around the average ocean temperature of 5°C and a salinity of 35 salinity units. The results are presented in the right column of figure 3 for the same parameters as the left. The ranges of oscillations are clearly greater. Since oscillations occur even at $Pr = 4$, another group of calculations has values of Pr increasing from 1 up to 128 (figure 4). The oscillations in all cases introduce
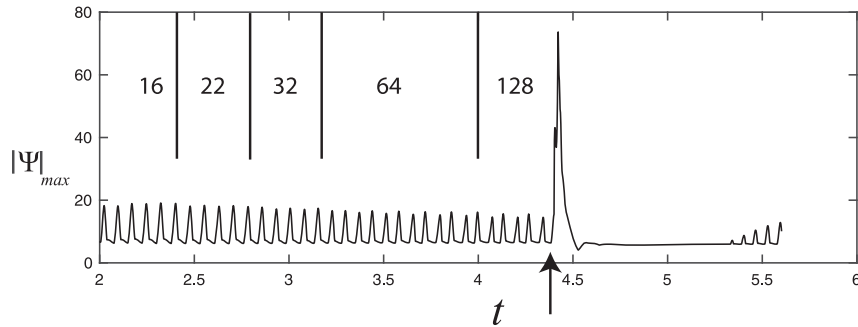

Figure 4 A run showing oscillations in streamfunction strength at different values of Pr at $Ra = 10^5$, $Raf = 3 \quad 10^5$, $L/D = 8$. At the times $t = 2$, 2.4, 2.8, 3.2 and 4.0, Pr takes the values 16, 22, 32, 64, and 128. Then, at $t = 4.4$, Raf is changed to 2.5 $\quad 10^5$ and after about one time unit a spontaneous growing oscillation becomes large enough to see.

the possibility that oscillations with the seawater equation of state might even occur in the limit of Stokes flow ($Pr = \infty$). Our numerical procedures cannot be altered for this limit, so the question of whether oscillations occur for a nonlinear density relation like seawater for Stokes flow in this container with Dirichlet/Newmann driving remains unresolved.

The time-dependent flows found here only occur in flows driven by a sinking salty plume. Flow speed increases and decreases as the sinking salty plume migrates back and forth a short distance from the warm salty end. The cycle is periodic. An oscillation in seawater with Ra and Raf close to the transition values to steady flow at $Pr = 10$ is shown in figure 5. The oscillation typically has a burst cycle with faster flow that deposits a plume of warm salty water along the bottom separated from a period of relatively constant flow speed with sinking that is not concentrated at the warm end. After the burst, a salty gravity current travels along the bottom.
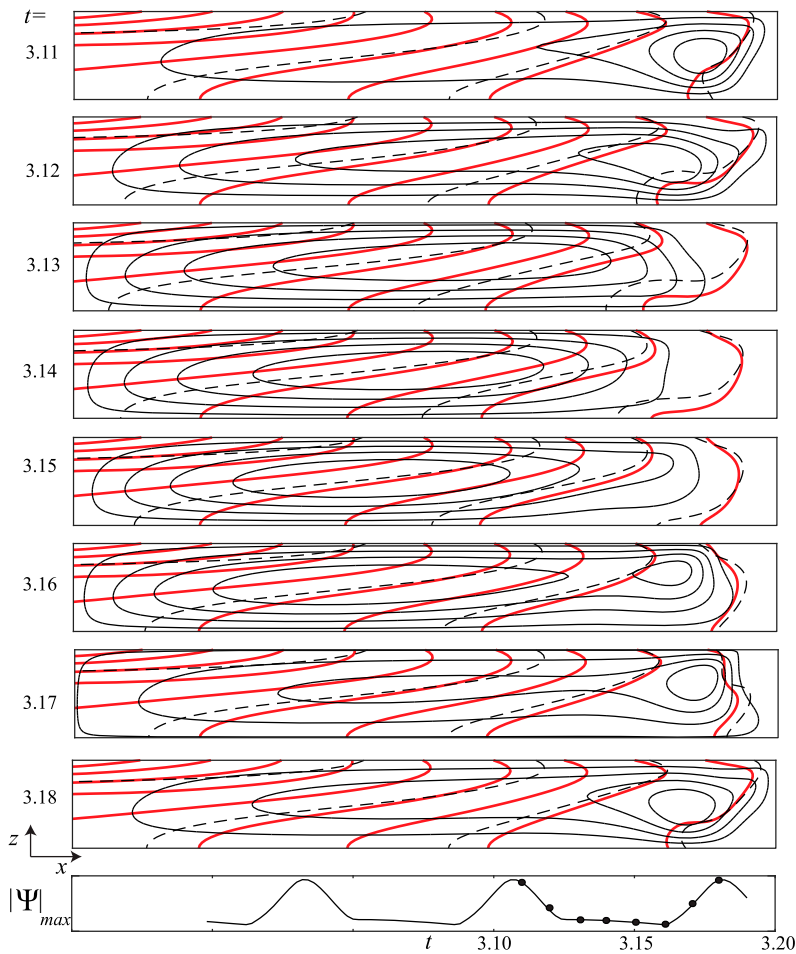

Figure 5 Vertical sections with contours of $|\psi|$ (black, solid), T (red, heavy) and S (black, dashed) during an oscillation with seawater properties. $Ra = 10^5$, $Raf = 3.5 \quad 10^5$, $Pr = 10$, $L/D = 8$ (colour online).
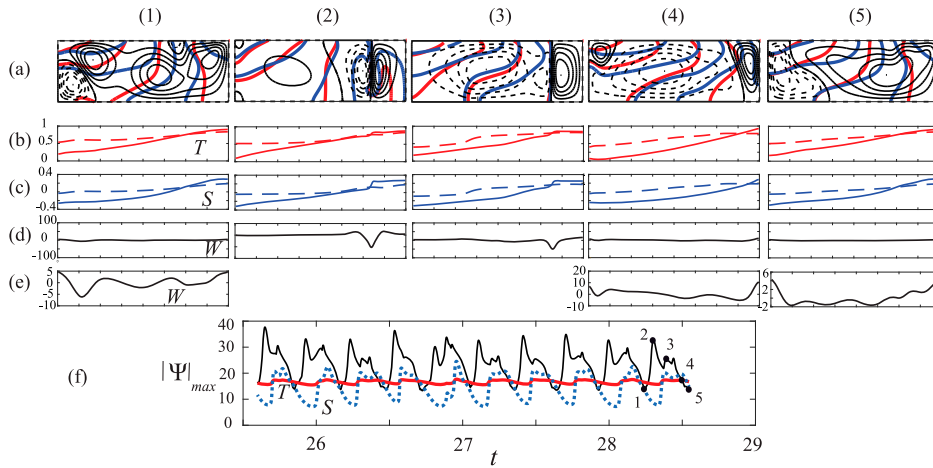
Figure 6 Columns (1–5) show a sequence during an oscillation cycle with $Ra = 10^5$, $Raf = 2.5 \times 10^5$, $L/D = 8$, and $Pr = 1$. Labelled dots in (f) give the time of each column (the interval is not exactly uniform). Rows: (a) Vertical sections showing contours of $|\psi|$ for counterclockwise circulation, (black, solid), $|\psi|$ clockwise circulation, (black, dashed), T (red, heavy) and S (blue, solid). Vertical axis stretched by approximately 2 so the details are more clearly viewed. (b) Distribution of T at depth of 0.1875 under the surface (red, solid) and along the bottom (red, dashed). (c) Distribution of S at the surface (blue, solid) and along the bottom (blue, dashed). (d) Distribution of vertical velocity W at middle depth. The panels all have the same scale. (e) Distribution of vertical velocity at middle depth with the scale of each panel normalised to the greatest value to show the slower flow. (f) Time sequence during many cycles of $|\psi|_{max}$ (black), T at the middle of the bottom (red), and S at the middle of the bottom (blue) (colour online).

The large amplitude version of the oscillation with seawater at $Ra = 10^5$, $Raf = 2.5 \times 10^5$, and $Pr = 1$ is a bit more complicated (figure 6). The flow speeds up and slows down as a plume of salty water alternately forms about 1/3 of the way from the warm end and then vanishes. The columns show time sequences of a variety of features. In column 1, the fast flow begins when a density inversion forms over the salty end and initiates a small surface gyre. The surface convergence makes a plateau of warm salty water that is separated from the stratified water by a distinct lateral jump in T and S surrounded by two counter-rotating gyres. During this period, the positive destabilising salt flux is not counterbalanced by a stabilising heat flux because the water in the warm pool under the surface at the right is already warm. The salty plume descends to the bottom in column 2 in a burst of negative vertical velocity. Then, salty warm water spreads to the left along the bottom (column 3). The bottom salty plume moves large lateral distances. A period follows with a weak sinking thermal plume that forms and then vanishes at the cold end (columns 4, 5). It is episodic and slightly irregular rather than periodic (figure 6(f)). For such low Pr, the spreading plumes appear to the eye to be laterally spreading bores along the bottom, but the structures have not always been visible and their detailed form and the parameters for which they are most pronounced is incomplete. A similar flow has been seen for Ra up to 2×10^6 and $Raf = 10^6$ but for only one cycle because of the long time required for the computation.

3 1 Steady flows in short containers

The aspect ratio $L/D = 2$ is wide enough to allow at least two convection cells lying side by side but narrow enough to exclude numerous cells along the container. Numerical runs at fixed Ra and with many differences in Raf are all conducted for $Pr = 1$ and ∞ until reaching either steady amplitude or the constant amplitude oscillations in the previous section. With $Pr = \infty$ the flows exhibit steady flows and the anticipated hysteresis and abrupt transitions for large Ra and Raf. Figure 7 shows values of T and S, at the middle of the container bottom along with maximum value of the streamfunction $|\psi_{max}|$ over wide ranges of Raf for the three values $Ra = 10^4, 3 \quad 10^4$ and 10^5. The two flow modes are the same as those in Stommel's box model (1961), with either a T-mode with sinking at the cold freshwater
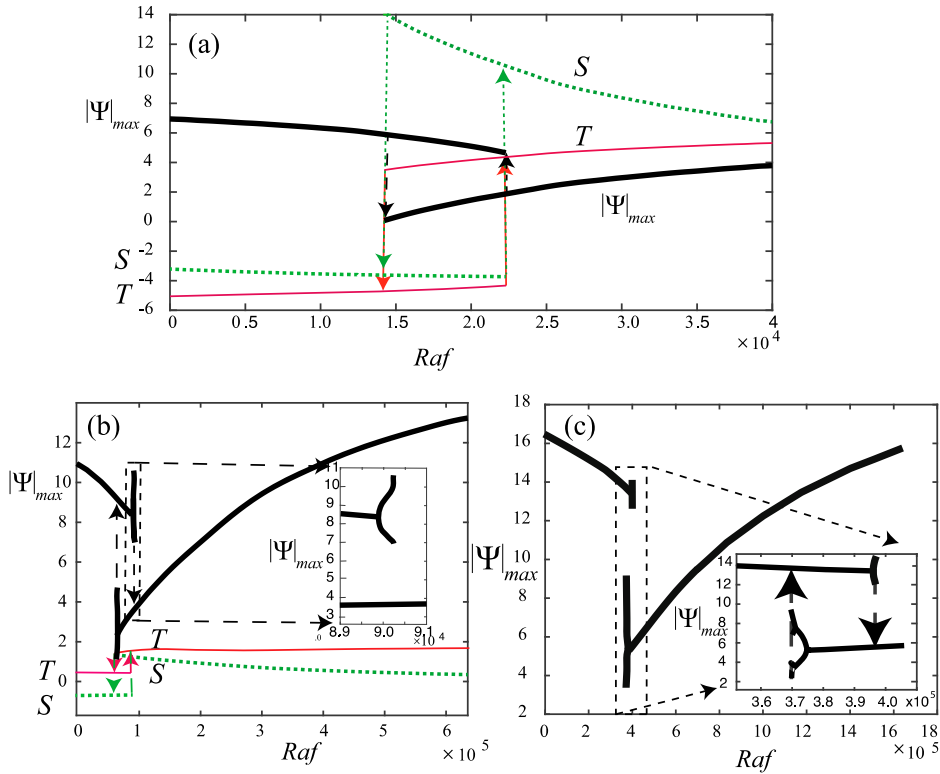

Figure 7 The maximum absolute values of streamfunction $|\psi_{max}|$ (black, heavy), values of T at the centre of the bottom (red, thin) and values of salinity S at the centre of the bottom (green, dotted) as a function of Raf for $Pr = \infty$ $L/D = 2$ and (a) $Ra = 10^4$, (b) $Ra = 3 \quad 10^4$, and (c) $Ra = 10^5$. T-mode is to the left and S-mode to the right. To avoid having the curves for $|\psi_{max}|$, T and S overlap, values are multiplied or offset as follows: (a), T has 0.5 subtracted and the result is multiplied by 20; S is multiplied by 200. (b), T is multiplied by 2; S is multiplied by 50. In (c) the T and S curves are omitted to give a closer view of $|\psi_{max}|$. The ranges of oscillation amplitudes near transitions are shown by the vertical curves. Insets in (b) and (c) show details of the amplitudes in the ranges where oscillations occur near transition. This is not a time sequence like figure 2. The oscillation curves give the maximum or minimum for a long run over numerous cycles (colour online).

end or an S-mode with sinking at the warm saltwater end. In addition, there are abrupt transitions accompanied by hysteresis between the two modes as found in the box model. A new feature absent in the box model is an oscillating flow that occurs near transition at the two larger values $Ra = 3 \quad 10^4$ and 10^5. These oscillations are indicated by vertical lines near the transition tips in the lower two panels of figure 7. Some oscillations are simple harmonic oscillations of the amplitude, but others are more complicated, for example at $Ra = 10^5$, the oscillation develops many frequencies close to transition. At values of Raf closest to transition (figure 8(a)), bursts of oscillations occur. All oscillations are the result of two cells with opposing circulation both becoming activated near transition.

The steady flow has one cell with either a cold sinking plume of concentrated flow at the cold end or a warm salty plume of concentrated flow at the warm end. The resolution does not seem to be an issue since no qualitative dependence on grid size has been found. Runs with twice the resolution (64   128) exhibit the same flow patterns and the same properties of abrupt changes, hysteresis and oscillations near transition as the example with a 32   64 grid shown in figure 7. Naturally, the exact quantitative values of Ra and Raf for transition depend on resolution. For example, as Raf is slowly increased in a 32   64 container, the transition in figure 7(b) from the T-mode to the S-mode is at $Raf = 90245 \pm 5$. The value at transition in a 64   128 container is approximately 0.4   higher at 90610 ± 5. Many more comparisons like this indicate that the results shown in the various figures can be considered to be correct to within 1 .

3 2   Steady flows in long containers

The flows in section 3 were composed of one cell with the superposition of two lateral cells during transient situations. A longer container allows a greater range of wavelengths in the lateral direction so that more complex flows might arise. This is true even in the limit of $Ra = Raf = 0$ in containers with the relatively large length $L/D = 16$, where two modes occur. They have a different number of cells. Their properties arise from the density fields shown in figure 9. There are four noteworthy features in the temperature and concentration fields. First the lateral profile of temperature at top and bottom has a different shape than the salinity shape; second, top and bottom T and S profiles almost perfectly follow each other; third, end effects to the S field are much smaller than end effects in T; and fourth, the width of the region with end effects is much longer for S than for T. The latter two features are not completely intuitive since T and S have the same diffusivity. The differences are due only to the two different types of boundary conditions. The larger width for S presumably arises from the Neumann boundary condition because S diffuses up and down near each end but then it must diffuse over large lateral distances to the other end where it is removed. This does not hold for T. The Dirichlet boundary condition for T permits a distribution that simply mimics the profile along the top except for small corrections in the lateral direction from the side boundary condition. The time for diffusive adjustment of T and S is also different because S diffuses over large lateral distances.

Tiny motion at small values of Ra and Raf is driven by the T and S distributions shown in figure 9. In that limit, the flow advection has a negligible influence upon the T and S distributions. Because of the differences in T and S distribution shown in figure 9, two flows are possible depending on the relative sizes of Ra and Raf. Figure 10 illustrates flow at $Ra = 1000$, and $LRaf/D = 160$ where the flow is dominated by T. (To quantitatively take
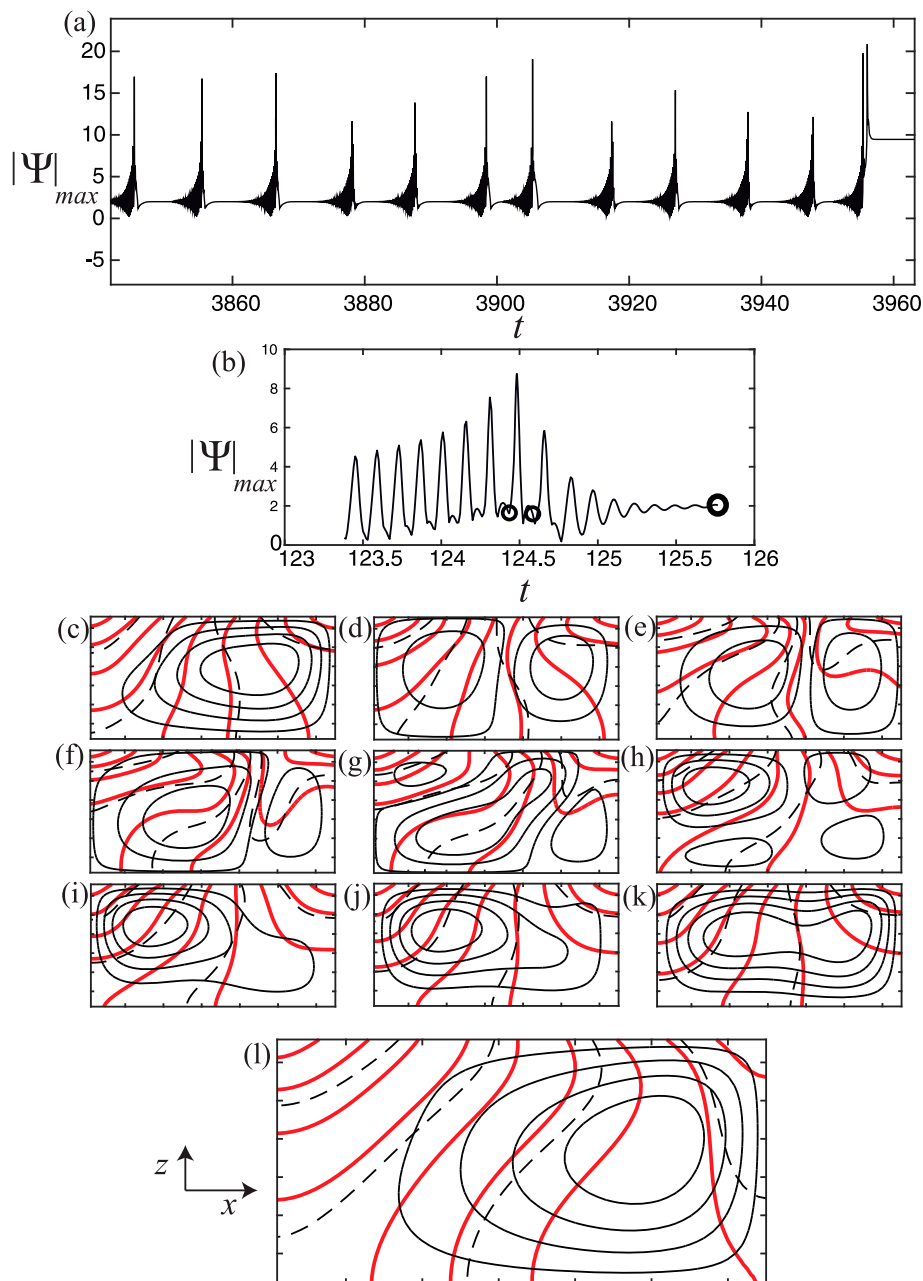
Figure 8 Maximum absolute value of streamfunction $|\psi_{max}|$ over time showing burst cycles for $Pr = \infty$, $L/D = 2$ and $Ra = 3 \quad 10^4$, and $Raf = 6 \quad 10^5$. These bursts occur when the convection is in the S-mode. (a) The transition of amplitude to the T-mode occurs after an adjustment down from to $Raf = 59{,}100$ is made at $t = 3955$. (b) In another experiment, $|\psi_{max}|$ shows many cycles during a burst. (c–k) Elevation views of $|\psi|$ contours (solid), T (red) and S (dashed) over the course of one cycle enclosed by the small circles on the left in (b). Time between panels is 0.025-time units. (l) Elevation view $|\psi|$ contours (black, solid), T (red, heavy) and S (black, dashed) for the relatively steady S-mode after the burst cycle has decayed away at the time indicated by the large circle in (b) (colour online).
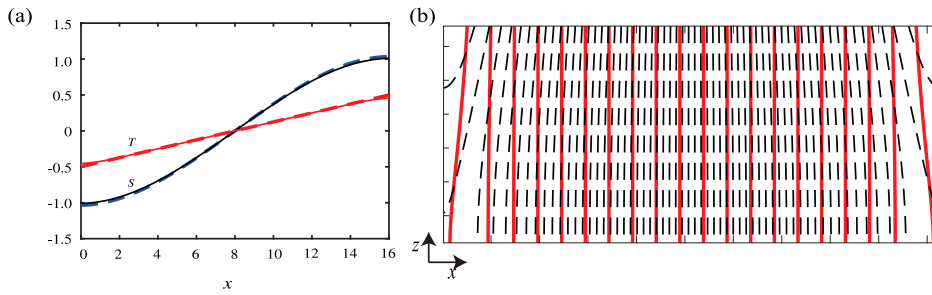
Figure 9 (a) The lateral distribution of T (red) and $10S$ (blue) at top (solid) and bottom (dashed) for $Pr = \infty, L/D = 16, Ra = Raf = 0$. (b) Vertical section with contours of T (red, heavy, every 0.05) and S (black dashed, every 0.025). The lateral direction of this long container is compressed by 4 (colour online).
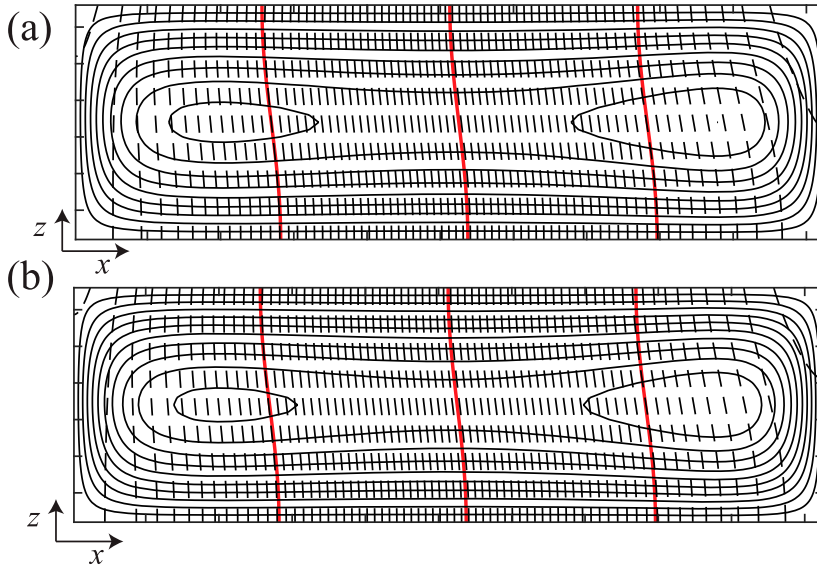

Figure 10 Laterally compressed (by 4) elevation views of contours of $|\psi|$ (black, solid), T (red, heavy) and S (black, dashed) for $Ra = 1000$ and $Raf = 10$, with $L/D = 16$ so that $LRaf/D = 160$. (a) $Pr = \infty$, (b) $Pr = 1$ (colour online).

account of the fact that the flux of S accumulates over larger lengths for larger L/D and that the flux from source to sink must diffuse laterally over larger distances, a better measure of the effect of the salt flux for large length is $LRaf/D$). The flow descends at the cold left end and rises at the warm right end. There is an enhanced closed circulation cell near each end because of the zero lateral flux required by diffusion of the temperature field at the sides. The flows for $Pr = \infty$ and 1 are almost identical.

The slow-motion dominated by salinity flux is considerably different. Figure 11 illustrates the flow at the same value with the larger value $LRaf/D = 800$. Convection is dominated by S and it has three cells. The flow shown has $Pr = \infty$, but the flow for $Pr = 1$ (not shown) is almost identical. History of flow development with isothermal and constant
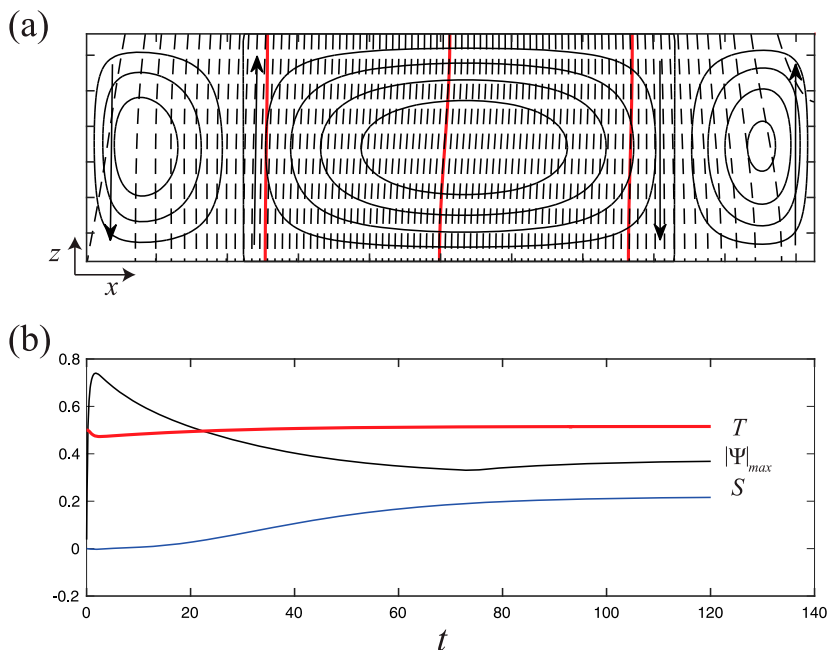
(a)

(b)

Figure 11 (a) Laterally compressed (by 4) elevation view of contours of $|\psi|$ (black, solid), T (red, heavy) and S (black, dashed) for $Ra = 1000$, $Raf = 50$, $L/D = 16$ so that $LRaf/D = 800$, and $Pr = \infty$. This is shown at $t = 120$, but subsequent changes are indistinguishable from this. (b) Evolution with time of $|\psi|_{max}$ (black), and bottom midpoints for T (red) and S (blue) (colour online).

salinity initial conditions is also different. Figure 11(b) shows evolution after the run commences from exactly zero flow, zero S, and $T = 0.5$. A measure of speed $|\psi|_{max}$ is plotted with time along with values of T and S at a point located exactly at the centre of the bottom. Initially, circulation grows driven by T conducting down into the container. Since S has to diffuse laterally greater distances to enter and leave the container, the field of S and the resulting buoyancy force increases more slowly. This results in the speed decreasing to a minimum at $t = 74$ and thereafter increasing as the S-dominated flow strengthens.

Therefore, even in the limit of very small amplitude, the two distinct T-mode and S-mode exist. When slowly changing Ra or Raf the transition between the two modes is not abrupt and there is no hysteresis. One of these two modes is always present in the numerous runs for small Ra as Raf is varied for $Pr = \infty$ and for $L/D = 4, 8, 16$, and 32. Abrupt transitions occur above a certain value of Ra as Raf is slowly varied, but exact values have not been determined. At $L/D = 8$, the abrupt transition emerges above approximately $Ra = 3600$. Transitions are fully abrupt and accompanied by hysteresis at three much larger values $Ra = 10^4$, 3×10^4 and $Ra = 5 \times 10^5$ (figure 12), where the most extensive exploration of parameter space was conducted.

Therefore, flow is characterised by significant hysteresis and multiple equilibria. In contrast to results with $L/D = 2$, for $Pr = \infty$ self-sustained oscillations are not found with Boussinesq fluid. However, in such cases when the value of Raf is close to the transition from an S-mode to T-mode and suddenly changed, even by a small amount, a decaying
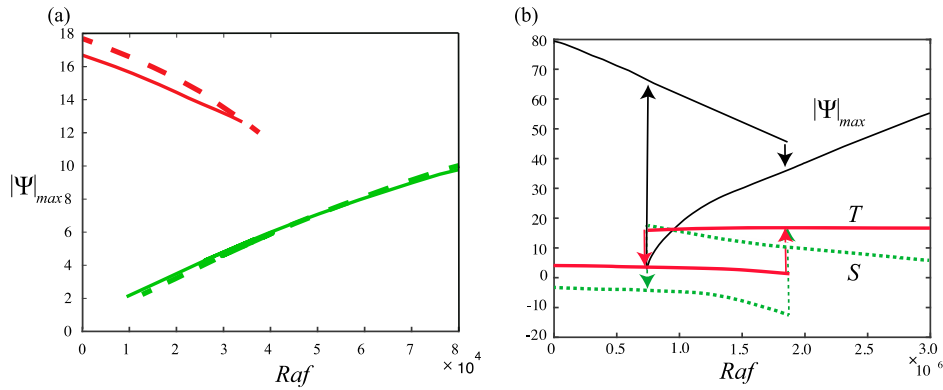
Figure 12 Amplitudes versus *Raf* for $L/D = 8$ (results are similar for $L/D = 16$ and 32). (a) Values of $|\psi|_{max}$ for $Pr = 1$ (dashed curves), $Pr = \infty$ (solid curves) at $Ra = 3 \quad 10^4$, for the *T*-mode (red) and *S*-mode (green). (b) $Ra = 5 \quad 10^5, L/D = 8, Pr = \infty$. Values of $|\psi|_{max}$ (black solid), *T* at the middle of the bottom (red, heavy), *S* at the middle of the bottom (green dashed) (colour Inline).

oscillation is found. This occurs for a wide range of values of *Ra* in a large number of runs, but coverage of parameter space with this occurring is not thoroughly mapped out. Typical examples of this oscillation are shown in figure 13, where the flow starts in the *S*-mode and *Raf* is decreased by steps of 100 down toward the transition value to the *T*-mode that occurs at $Raf = 9200$. The figure shows that when there is no additional change in *Raf* for two additional time units (point a in figure 13(b)), a steady flow (figure 13(a)) has developed. This flow pattern possesses a small *T*-driven counter cell at the cold end. All 11 additional downward steps in figure 13(b) have decaying oscillations, but each individual packet has slightly greater initial size as the transition value is approached. The sequence of panels for the growing oscillation (figure 13(c–g), with time shown in figure 13(i) shows that the oscillating flow develops small cells at each end that alternately strengthen and weaken. Then at $t = 193.55, Raf = 9200$ the transition to a *T*-mode occurs when a growing oscillation leads to instability (figure 13(h,j)). The amplitude becomes greater as the final transition to the *T*-mode occurs (figure 13(h)). The new cell with a much faster circulation that as sluggish in figure 13(g) grows from the cold end and spreads throughout the tank.

The transition from a *T*-mode to the *S*-mode also begins at the cold end but it does not oscillate. The cold thermal boundary layer migrates away from the cold end leading to a new cell that gradually grows and finally occupies the entire tank as an *S* mode (figure 14). The flow has a different structure in the *T* and *S* modes after they emerge from a transition. The *T*-mode (figure 13(g)) emerges with a warm boundary layer under the warm end with a relatively small lateral variation of *T* and *S* along the bottom. It has a similar structure before breaking down to an S-mode (figure 14(a)). The *S*-mode has a variation of *T* and *S* along the bottom with amplitude similar to the vertical amplitude in the boundary layer. This is true before transition to a *T*-mode (figure 13(a)) as well as after emerging from transition from a *T*-mode (figure 14(d)). In summary, both abrupt transitions start with flow reversal at the *T* end. The detailed reason for this is unknown.

For *Ra* and $Raf > 10^5$, both modes have boundary layers at the top that lie above deeper fluid with almost constant *T* and *S* like the present ocean. In some of the
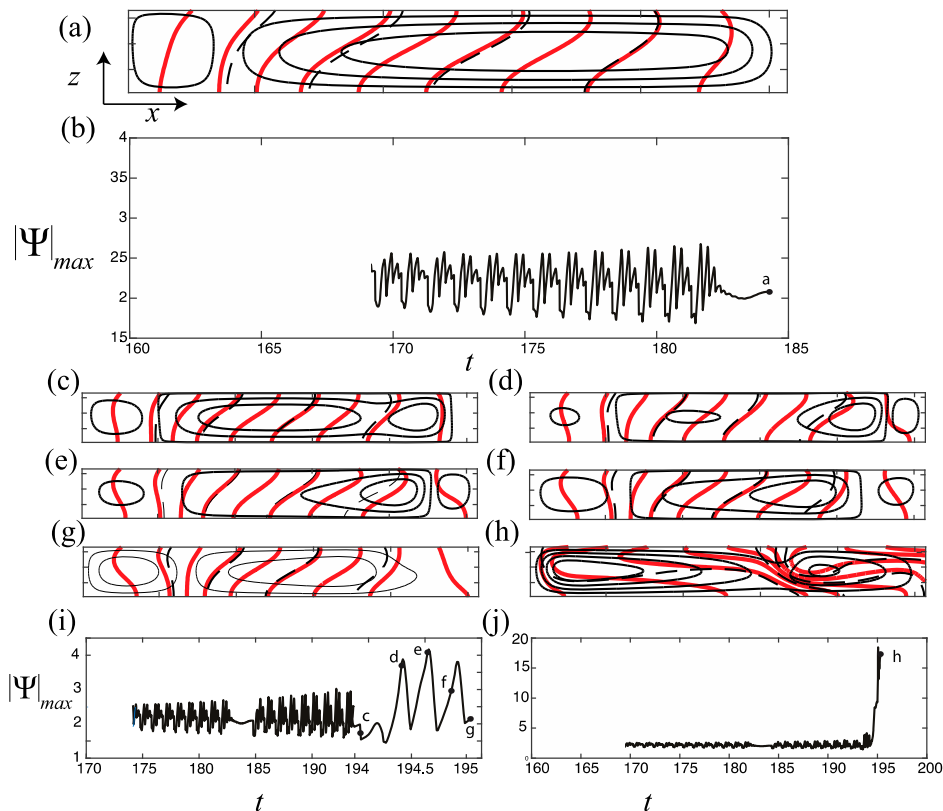
Figure 13 Transition from S-mode to T-mode for $Ra = 30{,}000$, $L/D = 8$, $Pr = \infty$. (a) A vertical section at $Raf = 10{,}300$ with contours of $|\psi|$ (black, solid), T (red, heavy) and S (black, dashed). (b) Time evolution of $|\psi|_{max}$ starting at $t = 169.4$ when $Raf = 11{,}600$ for 13 successive decreases in Raf by steps of 100 for one time unit each. The decrease is stopped for 2 time units at $Raf = 10{,}300$ ending in section (a). (c)–(h) Vertical sections at $Raf = 9200$ at the times shown in (i) (stretched axis) and (j) when a growing oscillation ending in transition to a T-mode occurs (colour online).

runs near a transition from one mode to the other, the deep regions tend to develop lateral changes along the bottom. The convection in figure 14(d) has a classic lateral convection-vertical diffusion balance that penetrates from top to bottom similar to estuary flow profiles by (e.g. Hansen and Rattray 1965). Although these offer promise as predictors for ocean transition, a systematic documentation near transition is not completed.

A notable feature is the presence of a small circular eddy near the sinking region for steady flow (figure 15). It occurs for both T-mode and S-mode flow, and it exists for values of Ra and $Raf > 10^3$. What drives this eddy? It appears to be a consequence of the fact that the sinking plume spreads out over the bottom making the fluid at the bottom flowing away from the plume to be stably stratified. This produces an upward restoring force away from the immediate region of sinking that leads to localised upwelling above the base of the spreading fluid.
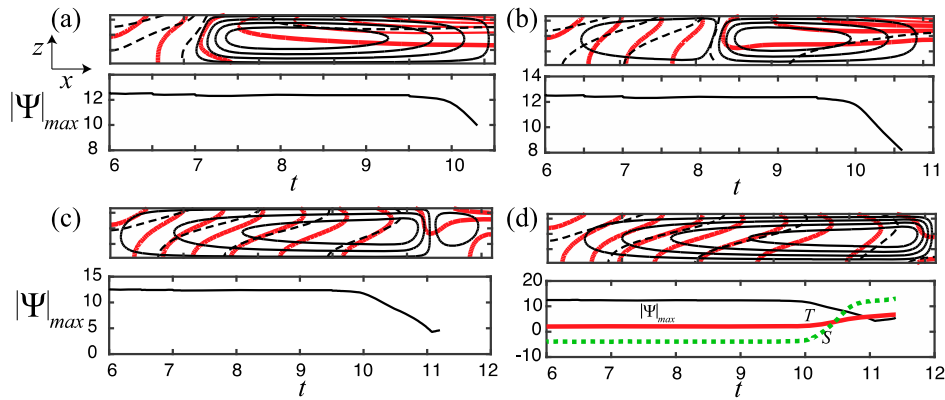
Figure 14 Transition from T-mode to S-mode at $Ra = 30{,}000$, $L/D = 8$, $Pr = \infty$. At $t = 9.5$, Raf was changed from 36,100 to 36,200. The upper panels in each pair are side views with contours of $|\psi|$ (black, solid), T (red, heavy) and S (black, dashed). The lower panels of (a)–(c) show a record of $|\psi|_{max}$. The lower panel in (d) adds records of T at the middle of the bottom multiplied by 10 and S at the middle of the bottom multiplied by 100 (colour online).
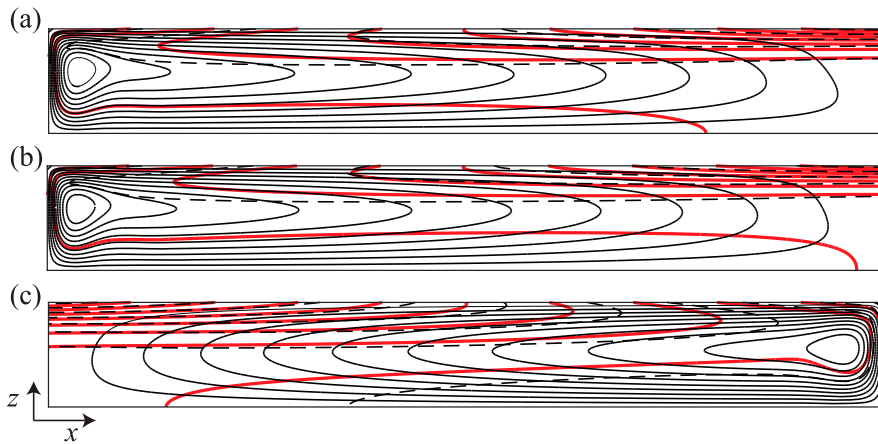

Figure 15 A vertical section with contours of $|\psi|$ (black, solid), T (red, heavy) and S (black, dashed). Flow with circular circulation near the sinking end for $L/D = 8$, $Pr = \infty$. (a) Pure T-mode, $Ra = 500{,}000$, $Raf = 0$. (b) $Ra = Raf = 500{,}000$, and (c) Pure S-mode, $Ra = 0$, $Raf = 500{,}000$ (colour online).

4 Conclusions

This convection, with a geometry of deep ocean overturning circulation, has two modes. It possesses some ranges of parameter space with hysteresis between the T-mode and the S-mode as in the Stommel box model, notably for $Pr = \infty$. Other ranges have oscillations, for example with Boussinesq fluid at $Ra = 10^5$ and $Pr < 4$, which is the parameter space that is covered most extensively with time-dependent flow. Another broad range of oscillations occurs with seawater, at the two values $Ra = 10^5$ and 3×10^5 for $Pr = 1$ up to $Pr = 128$. The oscillations occur spontaneously or can be triggered after a sudden change of a driving parameter such as Ra or Raf for parameters outside the range with spontaneous

oscillations. The oscillation consists of a strengthening and weakening of the overturning cell with significant sinking in the salty end as in the S-mode.

What does the cycle time of the oscillations imply for the ocean? The time scale of d^2/κ in the ocean has a value of about 3000 years using a depth of 3 km and the value for turbulent kappa of $10^{-4}\,\mathrm{m}^2\,\mathrm{s}^{-1}$. The oscillation in figure 6 has about four cycles during one-time scale and this corresponds to 750 years, with the fastest cycle of about 200 years for the cycles in figures 4 and 5. Therefore, this model recovers cycles that are close to millennial in the period. There is no sign of decadal cycles, although some of the oscillations near transition might be faster. The oscillations that occur only in small ranges near transition as in figure 7 are very hard to obtain and hold because of the narrow range of parameters for their existence. During the cycle, one or more cells might exist during part of a cycle. The closest agreement for all of the cycling flows to previous work are the oscillations in a convectively modified two box model (Colin de Verdière 2007), where Stommel's oscillatory S-fixed point generates an oscillation that is amplified by E–P. We have not analysed the nature of our bifurcations to the extent of testing whether the modes are infinite period as predicted there, because that would require a focused study.

However, the present results do not agree with the oscillations in the box model of Colin de Verdière, Jelloul, and Sèvellec (2006). In that 3 2 model, the oscillation consists of two modes, one is a heat transfer mode with direct flow from the polar box to the tropical box (T–T), the other mode has sinking in both ends with rising in the mid-latitude box (S–T) that short-circuits the global heat flow. The third mode, sinking in the tropics (the S–S) does not partake in the oscillation. Instead, the present results resemble an interaction of the S–S mode and the S–T mode. It was emphasised that assorted distributions of E–P (the equivalent of salt flux in our problem) would be more or less prone to oscillate. We have not investigated a variety of surface distributions for comparison with such results. Our oscillations also have differences from the cycles seen for ocean model flows. Since ocean models are much more complex than the convection studied here, they contain additional factors such as rotational constraints, wind stress, geometric complexity of the actual ocean basins, and ice dynamics (Winton and Sarachik 1993, Paul and Schultz 2002, Arzel *et al*. 2006). Most have vigorous T-mode oscillations, but the present oscillations seem to be more like S-mode oscillations than T-modes. In fact, there are no signs of speeding up and slowing down of T-mode oscillations in the present results even though Winton and Sarachik (1993) present a simple thermohaline loop model that illustrates oscillations in the T-mode that could conceivably apply generally. In addition, Arzel *et al*. (2006) also find oscillations in an ocean model with both heat flux and E-P top boundary conditions, so T–S oscillations occur in ocean model convection without Dirichlet–Neumann forcing too.

Of course, oscillating convection occurs in a number of convection problems in engineering. For example, growing oscillatory instability is found in Dirichlet/Newmann driving within tilted slots (Tsitverblit 2007). Those oscillations are easily understood as the interplay of convection cells and a larger scale overturning motion as they grow together. However, finite amplitude oscillations are unexplored for this geometry. It is thought that the growing oscillations eventually saturate to steady circulation at finite amplitude.

This model clearly lacks many aspects that control the dynamics of ocean circulation such as topography, rotation dynamics, planetary shape, and localised mixing, as discussed for example by Rossby (1998). Even our simplification is not quantitatively in the ocean

domain. Our model has an aspect ratio up to 32, and Ra up to 2×10^6 while the ocean has an aspect ratio of 10^3, and Ra is 10^{13}. Other models of this type have achieved Ra up to 10^9 but with similar small aspect ratios (Wang and Hwang 2005). Probably because of these factors, earlier studies with the present geometry and dynamics (Beardsley and Festa 1972, Rossby 1998, Hughes and Griffiths 2008) did not attempt to make a direct comparison of model results with the ocean as has been done here for the cycle time. It is not possible to mathematically show what happens in calculations with ocean aspect ratios of 10^3, but one expects that no new dynamics is introduced to this viscous model.

In addition, it must be mentioned that our oscillation does not resemble the oscillation in the laboratory experiments (Whitehead *et al.* 2005). The laboratory oscillation has a cycle starting with a freshwater layer cooled from above that is fully mixed internally but with an interface being mixed with deeper salty warmer water. The chamber is connected to an external chamber with a surface layer of fresh water lying above salt water at a constant temperature. The connection is through three tubes. The layer gradually deepens and becomes saltier after the layer reaches the middle tube where the flow that was initially out of the chamber reverses to become an inflow. Eventually, the layer mixes away and then it is replaced by the formation of a new freshwater layer as water flows in through the top tube. The laboratory cycle is similar to Welander's (1982) model of a layer cooled from above subjected to a freshwater flux but not very similar to the cycles in this or the other numerical models.

A sinking plume with turbulence present, presumably driven by turbulent shear instability has been seen in many numerical and laboratory experiments. The numerical runs here don't seem to be in a range with large enough Reynolds number Re for shear instability. Figure 3 can be used to estimate the size of Re. If $Re > 10^3$, the sinking plume can be expected to become turbulent and generate time-dependent flow. Scaling indicates that for $Pr = 1$, $Re = N|\psi|_{\max}/P$ where P is the number of grid points from the point of the maximum (the centre of the circular eddy) to the wall and N the number of vertical grid points. In the case of figure 3 the fastest flow with $Pr = 1$ oscillates with $|\psi|_{\max} = 40$, and this was at grid point $P = 21$, with one length scale of $N = 64$ grid points, so $Re = 127$. Flows have been calculated up to $Ra = 2 \times 10^6$ with smaller lengths using both 128×257 and 256×512 grids and the greatest value uses the shear next to the left-hand wall. The largest value of Peclet number Pe is found in the T-mode of the flow in figure 15 and it is $Pe = 960$. Thus, little prospect exists here of obtaining the effects of very large Ra (Paparella and Young 2002 Winters and Young 2009), and observing turbulence from plumes at large Re along with the implications thereof as reported by Mullarney *et al.* (2004), Siggers *et al.* (2004), Hughes and Griffiths (2006, 2008), Hughes *et al.* (2007), Scotti and White (2011), Gayen *et al.* (2013), Griffiths *et al.* (2013), Hughes *et al.* (2013), and Passaggia *et al.* (2017).

Clearly, there is a long way to go before thermohaline ocean oscillations are thoroughly understood. The present results along with laboratory observations of oscillating T/S and the oscillations in binary convection make it clear that T/S oscillations can occur in real physical fluids. Therefore, so far, they continue to be a potential candidate for oscillations in the Holocene (Paul and Schultz 2002). Whether they exist in the ocean at present or in the past, or whether they might occasionally occur in some T/S estuary system has not be verified by direct observation in the ocean. The oceans of the world remain greatly undersampled in spite of enormous progress in specialised areas. Notwithstanding, this contribution can be added to the list of increasingly strong arguments for continuing the studies

of the apparently simple but surprisingly fruitful consequences of Dirichlet/Neumann T–S forcing.

Acknowledgements

I thank Olivier Marcal for helpful discussion and useful suggestions.

Disclosure statement

No potential conflict of interest was reported by the authors.

References

Arzel, O., Colin de Verdiere, A. and England, M.H., The role of oceanic heat transport and wind stress forcing to abrupt millenial-scale climate transitions. *J. Climate*. 2010, **23**, 2233–2255

Arzel, O., Huck, T. and Colin de Verdiere, A., The different nature of interdecadal variability of the thermohaline circulation under mixed and flux boundary conditions. *J. Phys. Oceanogr*. 2006, **36**, 1703–1718.

Beardsley, R.C. and Festa, J.F., A numerical model of convection driven by a surface stress and non-uniform horizontal heating. *J. Phys. Oceanogr*. 1972, **2**, 444–455.

Colin de Verdière, A., A simple model of millennial oscillations of the thermohaline circulation. *J. Phys. Oceanogr*. 2007, **37**, 1142–1155. doi:10.1175/JPO3056.1.

Colin de Verdière, A., Ben Jelloul, M. and Sévellec, F., Bifurcation structure of thermohaline millennial oscillations. *J. Climate*. 2006, **19**, 5777–5795. doi:10.1175/JCLI3950.1.

Colin de Verdière, A. & Te Raa, L., *Clim. Dyn*. 2010, **35**, 1237–1256. doi:10.1007/s00382-009-0675-8.

Delworth, T., Manabe, S. and Stouffer, R.J., Interdecadal variations of the thermohaline circulation in a coupled osean-atmosphere model, *J. Climate*. 1993, **6**, 1993–2011.

Gayen, B., Griffiths R.W., Hughes, G.O. and Saenz, J.A., Energetics of horizontal convection. *J. Fluid Mech*. 2013, **716**, R10. doi:10.1017/jfm.2012.592.

Griffiths, R.W., Hughes, G.O. and Gayen, B., Horizontal convection dynamics: Insights from transient adjustment. *J. Fluid Mech*. 2013, **726**, 559–595.

Hansen D.V. and Rattray, M., Gravitational circulation in straits and estuaries. *J. Mar. Res*. 1965, **23**, 104–122.

Hughes, G.O., Gayen, B. and Griffiths R.W., Available potential energy in Rayleigh–Benard convection. *J. Fluid Mech*. 2013, **729**, R2, 1–10.

Hughes, G.O. and Griffiths, R.W., A simple convective model of the global overturning circulation, including effects of entrainment into sinking regions. *Ocean Model*. 2006, **12**, 46–79.

Hughes, G.O. and Griffiths, R.W., Horizontal convection. *Ann. Rev. Fluid Mech*. 2008, **4**, 185–208.

Hughes, G.O., Griffiths, R.W., Mullarney, J.C. and Peterson, W.H., A theoretical model for horizontal convection at high Rayleigh number. *J. Fluid Mech*. 2007, **581**, 251–276.

Loving, J.L. and Vallis, G.K., Mechanisms for climate variability during glacial and interglacial periods. *Paleoceanography*. 2005, 20, PA4024. doi:10.1029/2004PA00111.

Marchal, O., Jackson, C., Nilsson, J., Paul, A. and Stocker, T.F., Buoyancy-driven flow and nature of vertical mixing in a zonally averaged model. In *Ocean Circulation: Mechanisms and Impacts*, edited by A. Schmittner, J.C. Chiang and S.R. Hemming, 2007, Geophysical Monograph 173 (American Geophysical Union: Washington, D.C.). doi:10.1029/173GM05.

Marotzke, J., Ocean models in climate problems. In *Ocean Processes in Climate Dynamics: Global and Mediterranean Examples*, edited by P. Malanotte-Rizzole and A.R. Robinson, 1994, pp. 79–109 (Kluwer Academic, Springer, New York, NY).

Mullarney, J., Griffiths, R.W. and Hughes, G., Convection driven by differential heating at a horizontal boundary. *J. Fluid Mech*. 2004, **516**, 181–209.

Paparella, F. and W. Young 2002. Horizontal convection is non-turbulent. *J. Fluid Mech*. **466**, 205–214. doi:10.1017/S0022112002001313.

Passaggia, P., Scotti, A. and White, B., Transition and turbulence in horizontal convection: Linear stability analysis. *J. Fluid Mech*. 2017, **821**, 31–58. doi:10.1017/jfm.2017.228.

Scotti, A. and White, B., Is horizontal convection really "non-turbulent"? *Geophys. Res. Lett*. 2011, **38**, 1609, doi:10.1029/2011GL049701.

Sevellec, F. and Fedorov, A.V., Unstable AMOC during glacial intervals and millennial variability: The role of mean sea ice extent. *Earth Planetary Sci. Lett*. 2015, **429**, 60–68. doi.org/10.1016/j.epsl.2015.07.022.

Sevellec, F., Thirerrt, H. and Mahdi, B.J., On the mechanism of centennial thermohaline oscillations. *J. Marine Res*. 2006, **64**, 3, 355–392. doi:10.1357/002224006778189608.

Stommel, H., Thermohaline convection with two stable regimes of flow. *Tellus*. 1961, **3**, 224−230.

Paul, A. and Schultz, M., Holocene climate variability on centennial-to-millennial time scales: 2. Internal and forced oscillations as possible causes. In *Climate Development and History of the North Atlantic Realm*, edited by G. Wefer, W. Berger, K.E. Behre and E. Jansen, pp. 55–73, 2002 (Springer-Verlag: Berlin, Heidelberg).

Report of, SCOR working group, Ocean-Atmosphere materials exchange (OAMEX): Report 44, Unesco, Paris, 1979, 41.

Rossby, H.T., On thermal convection driven by nonuniform heating from below: An experimental study. *Deep-Sea Res*. 1965, **12**, 9–16.

Rossby, H.T., Numerical experiments with a fluid heated non-uniformly from below. *Tellus A Dyn. Meteorol. Oceanogr*. 1998, 242–257. doi:10.3402/tellusa.v50i2.14523.

Sakai, K. and Peltier, W.R., A multi-basin reduced model of the global thermohaline circulation: Internal and forced variability with paleoclimatological implications. *J.Geophys.Res*. 1996, **1 1**, 535–562.

Siggers, J., Kerswell, R. and Balmforth, N., Bounds on horizontal convection. *J. Fluid Mech*. 2004, **517**, 55–70. doi:10.1017/S0022112004000497.

te Raa, L., 2001. Convective oscillations in a laboratory model, *GFD Fellows Report* 2001. Available online at: http://gfd.whoi.edu/proceedings/2001/PDF/rep_teraa.pdf (accessed 1 October 2018).

Timmermann, A., Gildor, H., Schultz, M. and Tziperman E., Coherent resonant millennial-scale climate oscillations triggered by massive meltwater pulses. *J. Climate*. 2003, **16**, 2569–2585.

Tsitverblit, N., Bifurcation phenomena in confined thermosolutal convection with lateral heating: Commencement of the double-diffusive region. *Phys. Fluids*. 1995, **7**, 718–736.

Tsitverblit, N., Multiplicity of equilibrium states in laterally heated thermosolutal systems with equal diffusivity coefficients. *Phys. Fluids*. 1999, **11**, 2516–2538.

Tsitverblit, N., Mechanism of finite-amplitude double-component convection due to different boundary conditions. *Phys. Lett. A*. 2004, **329**, 445–450.

Tsitverblit, N., Double-component convection due to different boundary conditions in an infinite slot diversely oriented to the gravity. *Ann. Phys*. 2007, **322**, 1727–1770.

Tsitverblit, N.A., The finger regime of double-diffusive convection with the equal diffusion coefficients and mixed boundary conditions. Double-Diffusive Processes 1996 Summer Study Program in Geophysical Fluid Dynamics. 1997a, Woods Hole Oceanographic Institution, 145.

Tsitverblit, N.A., On the nature of direct instabilities in double-component convection with different boundary conditions. *Phys. Fluids*. 1997b, **9**, 2458–2460.

Turner, J.S., *Buoyancy Effects in Fluids*, 367 pp, 1973. (New York: Cambridge University Press).

Wang, W. and Huang, R.X., An experimental study on thermal circulation driven by horizontal differential heating. *J. Fluid Mech*. 2005, **54** , 49–73.

Weaver A.J. and Sarachik E.S., Evidence for decadal variability in an ocean general circulation model: An advective mechanism, *Atmos.-Ocean*. 1991, **29**, 197–231. doi:10.1080/07055900.1991.9649403.

Weaver, A.J., Marotzke, J., Cummins, P.F. and Sarachik, E.S., Stability and variability of the thermohaline circulation. *J. Phys. Oceanogr*. 1993, **23**, 39–60. doi:10.1175/1520-0485(1993)023.

Welander, P., A simple heat-salt oscillator, *Dyn. Atmos. Oceans*. 1982, **6**, 233–242. doi:10.1016/0377-0265(82)90030-6.

Welander, P.A., New type of double-diffusive instability? *Tellus A*. 1989, **41**, 66–72. doi:10.3402/tellusa.v41i1.11821.x.

Whitehead, J.A., Thermohaline ocean processes and models. *Ann. Rev. Fluid Mech.* 1995, **27**, 89–114.

Whitehead, J.A., Multiple states in doubly-driven flow. *Phys. D.* 1996, **97**, 311–321.

Whitehead, J.A., Multiple T-S states for estuaries, shelves and marginal seas. *Estuaries.* 1998, **21**, 278–290.

Whitehead, J.A., Stratified convection with multiple states. *Ocean Model.* 2000, **2**, 109–121.

Whitehead, J.A., Abrupt transitions and hysteresis in thermohaline laboratory models. *J. Phys. Oceanogr.* 2009. **39**, 1231–1243.

Whitehead, J.A., Convection driven by temperature and composition flux with the same diffusivity. *Geophys. Astrophys. Fluid Dyn.* 2017, **111**, 229–248. doi:10.1080/03091929.2017.1333608.

Whitehead, J.A., Cotel, A., Hart, S., Lithgow-Bertelloni, C. and Newsome, W., Numerical calculations of two-dimensional large Prandtl number convection in a box. *J. Fluid Mech.* 2013, **729**, 584–602.

Whitehead, J.A., te Raa, L., Tozuka, T., Keller, J.K. and Bradley, K., Laboratory observations and simple models of slow oscillations in cooled salt-stratified bodies. *Tellus A.* 2005, **57A**, 778–809. doi:10.1111/j.1600-0870.2005.00150.

Winters, K.B. and Young, W.R., Available potential energy and buoyancy variance in horizontal convection, *J. Fluid Mech.* 2009, **629**, 221–230.

Winton M. and Sarachek, E.S., Thermohaline oscillations induced by strong steady salinity forcing of ocean general circulation. *J. Phys. Oceanogr.* 1993, **23**, 1389–1410.

Zhao, F.Y., Liu, D. and Tang, G.F., Multiple steady flows in confined gaseous double diffusion with discrete thermosolutal sources. *Phys. Fluids.* 2007, **19**, 107103.

Appendix 1 The equations and their integration

The container is numerically represented as a rectangular grid. Initially ψ, T, and S are zero in the grid points except that along the top row, temperature linearly changes from 0 at the left end to 1 at the right and salt flux linearly changes from -0.5 at the left to 0.5 at the right end. Since values of S are the result of flux boundary conditions, the drift in the mean value of salinity S within the container is zero, but numerically the mean remains zero only to the level of precision of the flux conditions. To ensure that the drift in the mean value is as small as possible, an external line of grid points is added outside each line of boundary grid points. This physically corresponds to a thin layer of stagnant material with the diffusivity of water around the container. In this layer, the desired value of S flux in or out of the container is imposed by pure diffusion. This produces precision to the salt budget at the numerical truncation order of 10^{-17}. Quality checks in numerous calculations verified that the average value of S randomly fluctuates about a value of $O(10^{-16})$ for all calculations presented in this paper for even thousands of diffusive times since the salt flux in balances the salt flux out at the top. This method of diffusively imposing flux at the boundaries with the extra layer is superior by approximately 10 orders of magnitude to using one-sided difference equations to calculate the total flux of salinity around the boundaries. Heat flow through the sides and bottom is also much more accurately preserved using this method.

To advance in time, equations (1) and (2) for temperature, and salinity distributions are stepped forward using a leapfrog-trapezoidal scheme for each time step δt. Lateral flux of heat and salinity are set to zero through the two sides and through the bottom. The equation at each time step depends on whether Pr is finite or infinite. If Pr is finite, the vorticity calculation (3) is stepped ahead in time. For infinite Pr, no time step is needed and instead a standard Poisson equation solver is used for (3). In both cases, (4) for streamfunction is solved using the same Poisson solver. In all cases, free slip (zero vorticity) and zero streamfunction is set on all four sides. The time step is repeated numerous times to find the evolution of the temperature, salinity and velocity fields.

Naturally, smaller grid sizes and time steps improve the precision of the results. In these calculations, no dependence has been found between the qualitative results shown here and results with smaller grid sizes, although clearly the quantitative values converge with finer grid size to an asymptotic value. This was also true in previous calculations with the same numerical scheme (Whitehead *et al.* 2013, Whitehead 2017). For a quantitative example, at $Ra = 10^6$ the vorticity in a square 64×64 grid has the same pattern but a maximum value that is $\sim 1.8 \times$ higher than vorticity

on a 128 grid at the same instant, and that value is ~ 0.6 higher than a 256 grid (Whitehead *et al.* 2013). The precision of the test results is very close to the precision in Rossby's results (1998). Such results can be anticipated to only occur in the absence of shear instability. If internal speeds are large enough for Reynolds number *Re* based on the speed to attain a size of 100 or more, shear instability will occur and the fluctuations will be more energetic with finer resolution. The present calculations are not conducted with large enough *Re* for this to be true.